

We are IntechOpen, the world's leading publisher of Open Access books Built by scientists, for scientists

6,900

Open access books available

186,000

International authors and editors

200M

Downloads

Our authors are among the

154

Countries delivered to

TOP 1%

most cited scientists

12.2%

Contributors from top 500 universities



WEB OF SCIENCE™

Selection of our books indexed in the Book Citation Index
in Web of Science™ Core Collection (BKCI)

Interested in publishing with us?
Contact book.department@intechopen.com

Numbers displayed above are based on latest data collected.
For more information visit www.intechopen.com



Aerosol Spray Pyrolysis Synthesis of Doped $\text{LiNi}_{0.5}\text{Mn}_{1.5}\text{O}_4$ Cathode Materials for Next Generation Lithium-Ion Batteries

George Ganas, George Karagiannakis, Aitor Eguia-Barrio, Miguel Bengoechea, Iratxe de Meatza and Georgia Kastrinaki

Abstract

The autonomy of next generation Electric Vehicles relies on the development of high energy density automotive batteries. $\text{LiMn}_{1.5}\text{Ni}_{0.5}\text{O}_4$ (spinel structure) is a promising active cathode material in terms of charge rate capability, theoretical capacity, cost and sustainability being a cobalt-free material. In the current study pristine and doped (Fe, Al, Mg) $\text{LiMn}_{1.5}\text{Ni}_{0.5}\text{O}_4$ particles were synthesized by an Aerosol Spray Pyrolysis pilot scale unit in a production rate of 100 gr h^{-1} and were evaluated for their electrochemical activity in Half Coin Cell form. The doped particles were characterized in terms of their surface area, particle size distribution, crystallite size, morphology and ion insertion of the doping element into the $\text{LiNi}_{0.5}\text{Mn}_{1.5}\text{O}_4$ lattice by Raman spectroscopy. The mixed oxide particles had homogeneous composition which is an inert characteristic of aerosol spray pyrolysis synthesis. The electrochemical activity of the material is attributed both to the nanoscale structure, by successful dopant ion insertion into the spinel lattice as well as to optimization of carbon and spinel particle interface contact in the microscale for increase of electrode conductivity.

Keywords: Li-ion batteries, aerosol spray pyrolysis, LNMO, spinel, cathode materials

1. Introduction

The unavoidable consumption of the global fossil fuel reserves in conjunction with the increasing environmental issues, have rendered the storage of electrical energy produced from renewable sources of greater importance than ever before [1]. Rechargeable Lithium-Ion batteries (LIB) have gained considerable attention among various energy storage technologies and are currently widely employed or considered to be deployed in electric devices, electric vehicles (EVs) and grid energy storage systems due to their relatively high energy density, high voltage, better cycle life and environmental friendliness [2–5]. Pyrolysis methods are extensively studied for the synthesis of anode and cathode materials for LIBs [6–11], either as mixed oxide particles [12, 13] or carbon-based structures [14], thereby providing a scalable and sustainable process for the production of electrode materials. The demand for high specific power, energy capacity [15, 16] and safety within the battery lifetime

has led to the importance of “going nano” [17] in order to optimize electrode electrochemical activity and stability towards lithium ion intercalation (insertion within the material lattice) in the framework of the necessary cycling operation.

Aerosol spray pyrolysis synthesis is an established and scalable method for the synthesis of metal oxides [18], metal [19] and carbon-based [20] materials. The atomized droplets undergo controlled evaporation of solvents and subsequent precipitation of precursor materials by regulating the operating conditions of the process to allow tuning of size distribution, morphology, porosity and to achieve uniform multicomponent composition of the synthesized particles and structures. Furthermore, the residence time of the droplets in the heated reactors is in the time frame of seconds, while further (i.e. post-synthesis) calcination can be performed in powder form. The precursor solutions for aerosol spray pyrolysis are mostly aqueous based, leading only to gaseous byproducts that can be in-line processed or captured, thereby contributing further to an environmentally sustainable and cost-effective process.

To meet the demanding battery standards, a wide variety of cathode materials has been thoroughly studied, such as the layered LiMO_2 [21–24], the olivine LiMPO_4 [25–27] and the spinel structure of LiM_2O_4 . Among the materials of the latter LiM_2O_4 family, $\text{LiNi}_{0.5}\text{Mn}_{1.5}\text{O}_4$ (LNMO) is considered a very promising candidate as a cathode material in both environmental [28, 29] and operational terms, since it exhibits an operating charge/discharge voltage of ~ 4.7 V vs. Li/Li^+ , a theoretical capacity of ~ 147 $\text{mAh}\cdot\text{g}^{-1}$ [30] and it does not require the use of cobalt. In this work we investigate the doping of Mg, Al and Fe through partial substitution of Ni in the LNMO structure (Mg-LNMO, Al-LNMO and Fe-LNMO respectively) via the Aerosol Spray Pyrolysis (ASP) synthesis technique for a production capacity of approximately 100 $\text{g}\cdot\text{h}^{-1}$. Subsequently, the doping effect on the electrochemical performance of LNMO half cells is assessed experimentally.

2. $\text{LiNi}_{0.5}\text{Mn}_{1.5}\text{O}_4$ spinel structure

LNMO can be formed in two different space groups as it is also exhibited in **Figure 1(a)** the single cubic $P4_332$ phase (ordered), where in the absence of Mn^{3+} the Mn^{4+} and Ni^{2+} ions are located at 12d and 4a sites of the lattice respectively, Li ions occupy the 8c sites and O ions the 8c and 24e sites and b) the face centered $Fd-3m$ phase (disordered) where Mn^{4+} and Ni^{2+} are randomly distributed at 16c sites of the lattice, while Li and O ions are located at 8a and 32e sites respectively [31]. $P4_332$ demonstrates a stoichiometric amount of oxygen atoms, while $Fd-3m$ presents oxygen vacancies, represented by the non-stoichiometric parameter δ . Thus, a $\text{LiNi}_{0.5}\text{Mn}_{1.5}\text{O}_{4-\delta}$ structure appears with certain Mn ions being reduced to Mn^{3+} due to charge balancing [32].

Despite the fact that LNMO exhibits promising electrochemical features, it may demonstrate significant capacity reduction during cycling due to Mn diffusion in the electrolyte mass, caused by various lattice modifications in conjunction with the Jahn-Teller effect [33]. Since the electrochemical performance of LNMO can be affected by the synthesis route and thus the stoichiometry, morphology, crystal structure and impurities [34], many synthesis methods have been employed in order to improve LNMO performance: hydrothermal route [35, 36], co-precipitation [37–40], sol-gel [41, 42], induction thermal plasma [43], molten salt [44–46], liquid phase self-propagating high-temperature synthesis (LPSHS) and aerosol spray pyrolysis [47].

The electrochemical performance of LNMO can be improved via cation doping [48–50] by Mg, Al and Fe. This approach contributes to LNMO lattice stabilization, increase of specific capacity, reduction of the $\text{Li}_x\text{Ni}_{1-x}\text{O}$ phase which is formed in

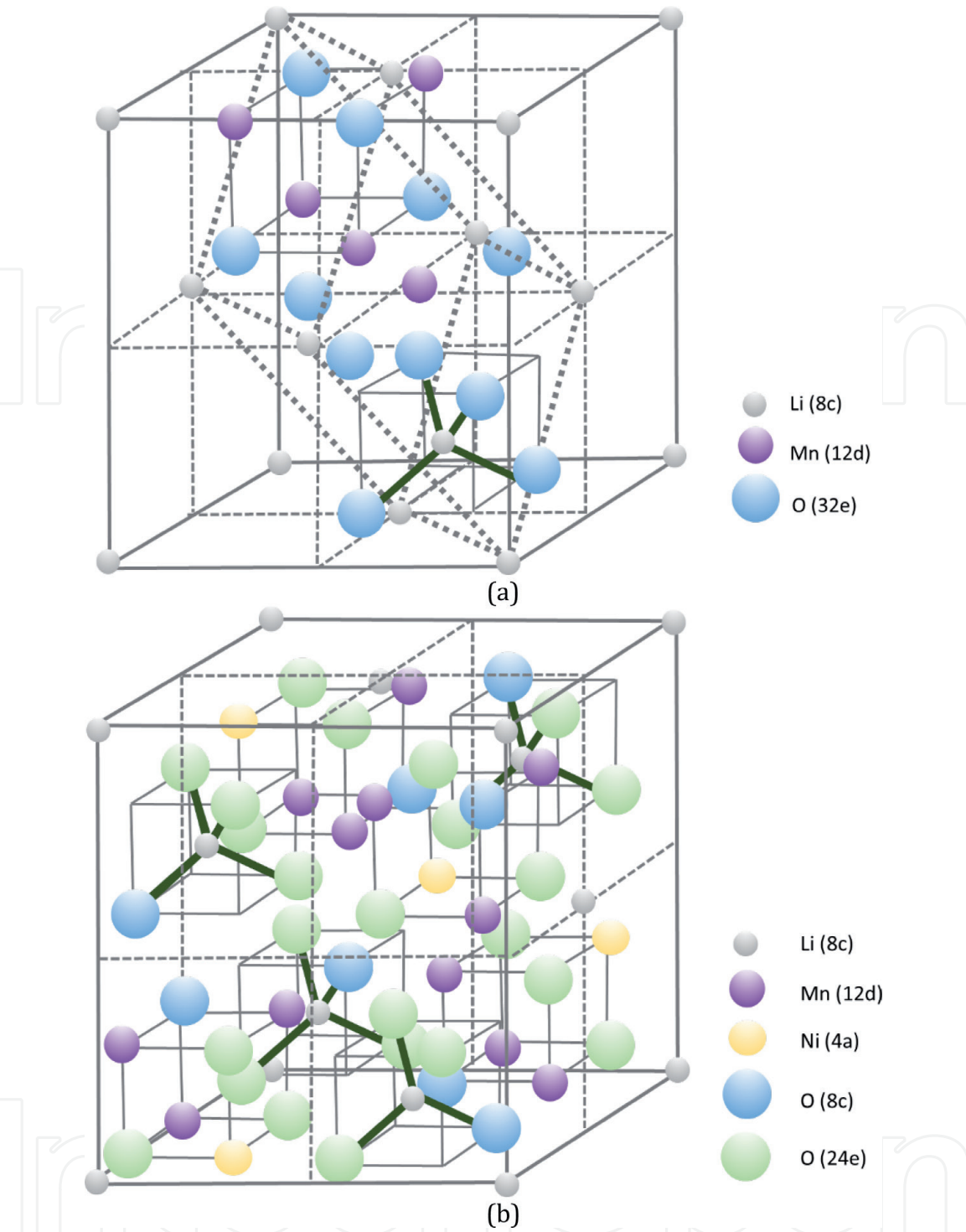


Figure 1.
Crystal phases of LNMO: (a) ordered $P4_332$, (b) disordered $Fd-3 m$.

the case of the disordered $Fd-3 m$ structure and increase of cycle life. Moreover, the doped compositions are less expensive, abundant and without scarcity or toxicity issues such as in the case of cobalt [51–58].

3. Experimental

3.1 Material synthesis

The LNMO material was synthesized by the Aerosol Spray Pyrolysis method [19], which utilizes the principles of bottom up synthesis in droplet micro-reactors.

A precursor solution is atomized into fine droplets which subsequently undergo evaporation of the solvent while transferred by a carrier gas, inside a heated tubular reactor. The advantages of the respective synthesis technique is the short production time of some seconds in the reactor zone and the scalability of the produced material quantities.

In the current synthesis campaigns, the precursor solution was a 1 M aqueous solution of LiNO_3 (Merck, $\geq 98\%$), $\text{Ni}(\text{NO}_3)_2 \cdot 6\text{H}_2\text{O}$ (Merck, $\geq 99\%$), $\text{Mn}(\text{NO}_3)_3 \cdot 4\text{H}_2\text{O}$ (Alfa Aesar, 98%), $\text{Mg}(\text{NO}_3)_2 \cdot 6\text{H}_2\text{O}$ (Sigma Aldrich, 98 + %), $\text{Al}(\text{NO}_3)_3 \cdot 9\text{H}_2\text{O}$ (Sigma Aldrich, $\geq 98\%$) and $\text{Fe}(\text{NO}_3)_3 \cdot 9\text{H}_2\text{O}$ (Merck, $\geq 99\%$), in molar ratios of Li:Ni:Mn:D: 1:0.5-x:1.5:x and the temperature of the heated reactor was 800°C . The collected powder was subsequently calcined at 850°C for 16 h (air atmosphere) in a muffle furnace in order to obtain the disordered phase of the LNMO material [11]. The temperature of the reactor controls the evaporation rate of the solvent and thus the chemical composition and morphology of the synthesized particles. The synthesis reactor is a pilot plant unit constructed and operated in CETH's facilities. In this study, 4 different materials were produced; the pristine LNMO and 3 metal doped LNMO compositions using Mg, Al and Fe as additives, namely Mg-LNMO, Al-LNMO and Fe-LNMO, respectively.

3.2 Structural characterization

The identification of the phase structure was performed by XRD analysis using a Siemens D500/501 X-ray diffractometer with $\text{Cu K}\alpha$ radiation between 5° and 80° at a scan rate of $0.040^\circ/\text{s}$. SEM/EDS analysis as well as the mapping of the materials were performed with a JEOL JSM-6300 microscope, while the TEM analysis was performed using a JEOL JEM 2010 high-resolution microscope. The ordered/disordered structure was identified with a Raman Renishaw microscope equipped with a 514 nm Argon laser of 50 mW. The specific surface area of the samples (BET method) was measured with the aid of a N_2 adsorption porosimeter (Micromeritics ASAP 2000, at 77 K, after degassing the samples at 250°C). Finally, the particle size distribution of the materials synthesized (powder form) was performed using a TSI PSD 3603 Particle Size Distribution Analyzer.

3.3 Electrode assembly and electrochemical characterization

The electrochemical performance of synthesized LNMO was evaluated at the laboratory scale by preparing electrodes and assembling half-coin cells (HCC). During the cathode formulation, an N-methyl-2-pyrrolidone (NMP) slurry was prepared, consisting in a first approach of 90 wt. % of active material with the rest 10 wt.% being carbon black (C-ENERGY Super C65 from IMERYS Carbon & Graphite) and Poly-Vinylidene Fluoride (PVdF HSV900 from Arkema) as electronic conduction enhancer and binder, respectively, while different ratios followed (84/8/8, 80/10/10) when issues were observed on the slurry stability and electrical conductivity of the electrodes. After coating the slurry on an aluminum current collector foil (Showa Denko, $20\text{ }\mu\text{m}$ thickness) using the doctor blade technique to a targeted loading of $1.0\text{--}1.5\text{ mA}\cdot\text{cm}^{-2}$, the resulted electrodes were dried at 120°C under vacuum overnight, and the coin cell assembly followed.

The electrochemical performance of the prepared electrodes has been analyzed by assembling and testing coin cells (CR2025, Hohsen), in HCC configuration using Li metal disk ($50\text{ }\mu\text{m}$ thick, Albermale) as counter anode electrode. One layer of polyolefin Celgard 2325 separator was used in all coin cells with $50\text{ }\mu\text{L}$ of 1 M LiPF_6 EC/EMC electrolyte from Arkema. The cells were tested in a potential window of 3.5-5 V at room temperature in a working C-rate range

between C/5 (5 h) and 5C (12 min). C-rate calculations were made based on a LNMO specific capacity of $135 \text{ mAh}\cdot\text{g}^{-1}$.

4. Physicochemical characterization results

Figure 2(a) depicts the XRD spectra of the synthesized LNMO materials. In all cases a desired well-crystallized $\text{LiNi}_{0.5}\text{Mn}_{1.5}\text{O}_4$ structure was obtained, with the characteristic peaks of the typical cubic structure at 19, 36, 44, 59, 64 2θ values; the higher resolution graph in **Figure 2(b)** referring to the pristine LNMO indicates two weaker peaks at ~ 37.5 and ~ 43.5 2θ values corresponding to the $\text{Li}_x\text{Ni}_{1-x}\text{O}$ phase.

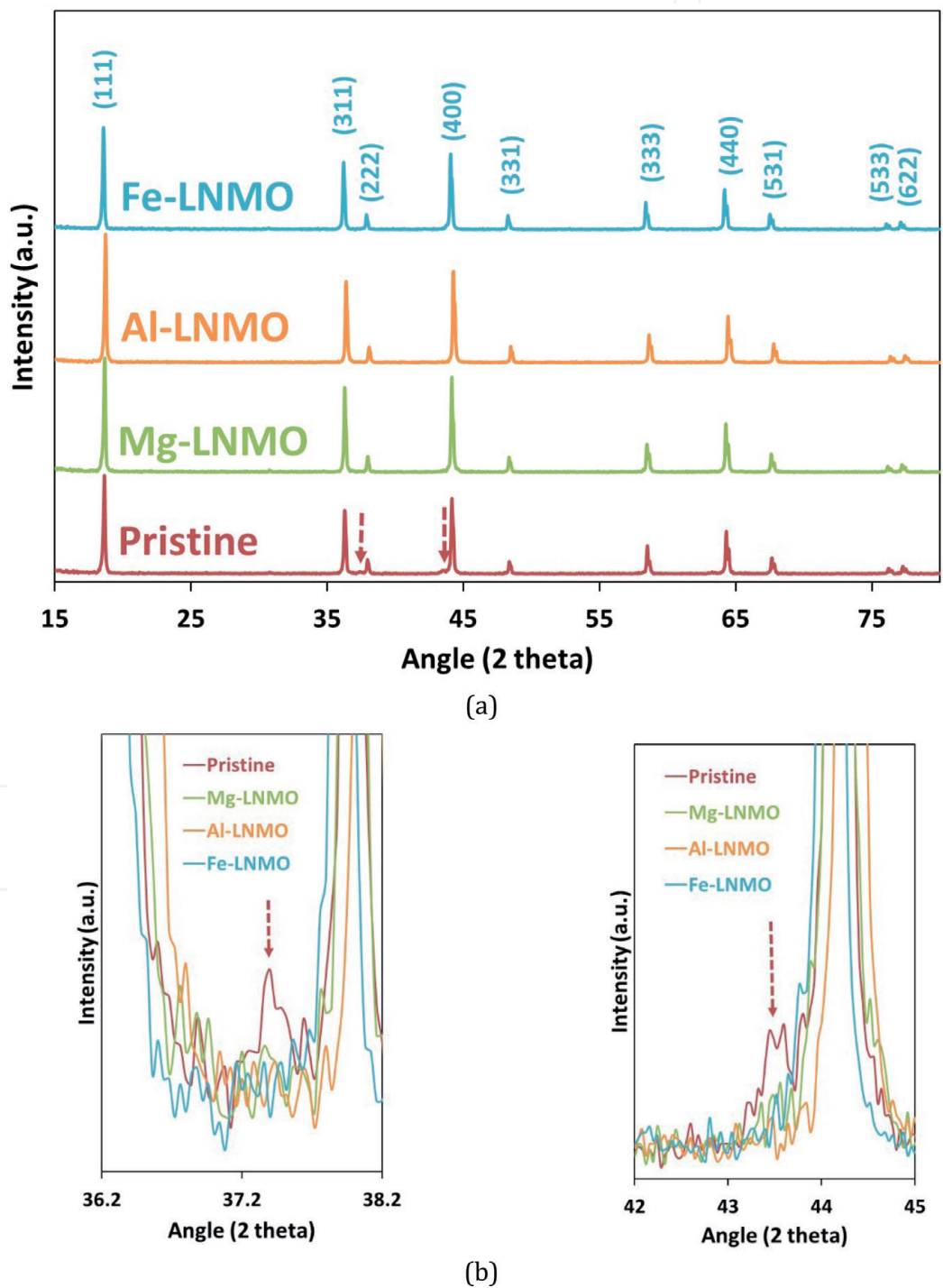
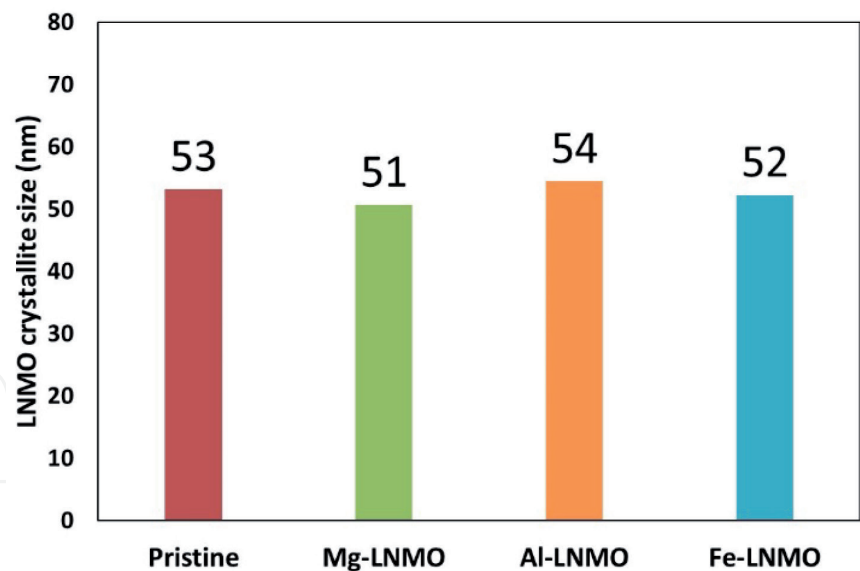
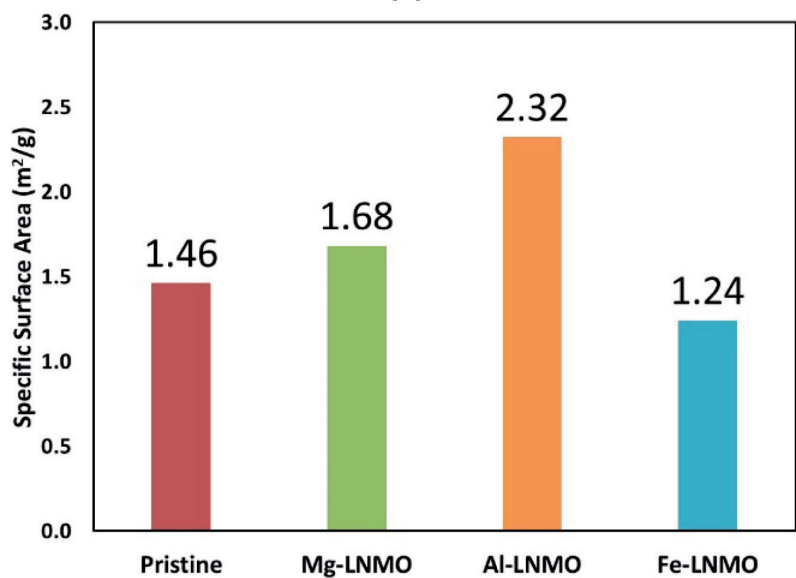


Figure 2.
(a) XRD of the pristine and doped $\text{LiNi}_{0.5}\text{Mn}_{1.5}\text{O}_4$ with Fe, Al and Mg materials (b) higher resolution XRD graph depicting the additional $\text{Li}_x\text{Ni}_{1-x}\text{O}$ of the pristine sample.



(a)



(b)

Figure 3.
Crystallite size (a) and specific surface area (b) of the doped LNMO materials.

On the contrary, in the case of doped LNMO compositions these peaks are not present, assuming, therefore, the elimination of the undesired $\text{Li}_x\text{Ni}_{1-x}\text{O}$ phase.

Crystallite size was calculated by the Scherrer's formula from the FWHM of the (111) $\text{LiNi}_{0.5}\text{Mn}_{1.5}\text{O}_4$ peak; the calculated sizes in **Figure 3(a)** exhibit crystallites with an average size of ~53 nm for all the materials. Doping seems to affect the specific surface area in a different manner; in **Figure 3(b)** the pristine sample exhibits a $1.46 \text{ m}^2\cdot\text{gr}^{-1}$ specific surface area which increases slightly to $1.68 \text{ m}^2\cdot\text{gr}^{-1}$ for Mg and significantly to $2.32 \text{ m}^2\cdot\text{gr}^{-1}$ for the Al sample, while in accordance to its crystallite size deviation the Fe sample exhibits lower surface area than the pristine at $1.24 \text{ m}^2\cdot\text{gr}^{-1}$. The different surface areas can be related to the morphology exhibited by SEM in **Figure 4**, where spherical particles seem to exhibit a non-dense, macro-porous structure. Particles synthesized by aerosol synthesis are expected to have a spherical morphology based on the aerosol process principle [19]. SEM images for the pristine and the doped particles depict multiple particulate aggregates forming the macroscopic spherical particles. The EDS mapping images show a homogeneous dispersion of the Ni, Mn and of the respective Mg, Al and Fe dopants per case,

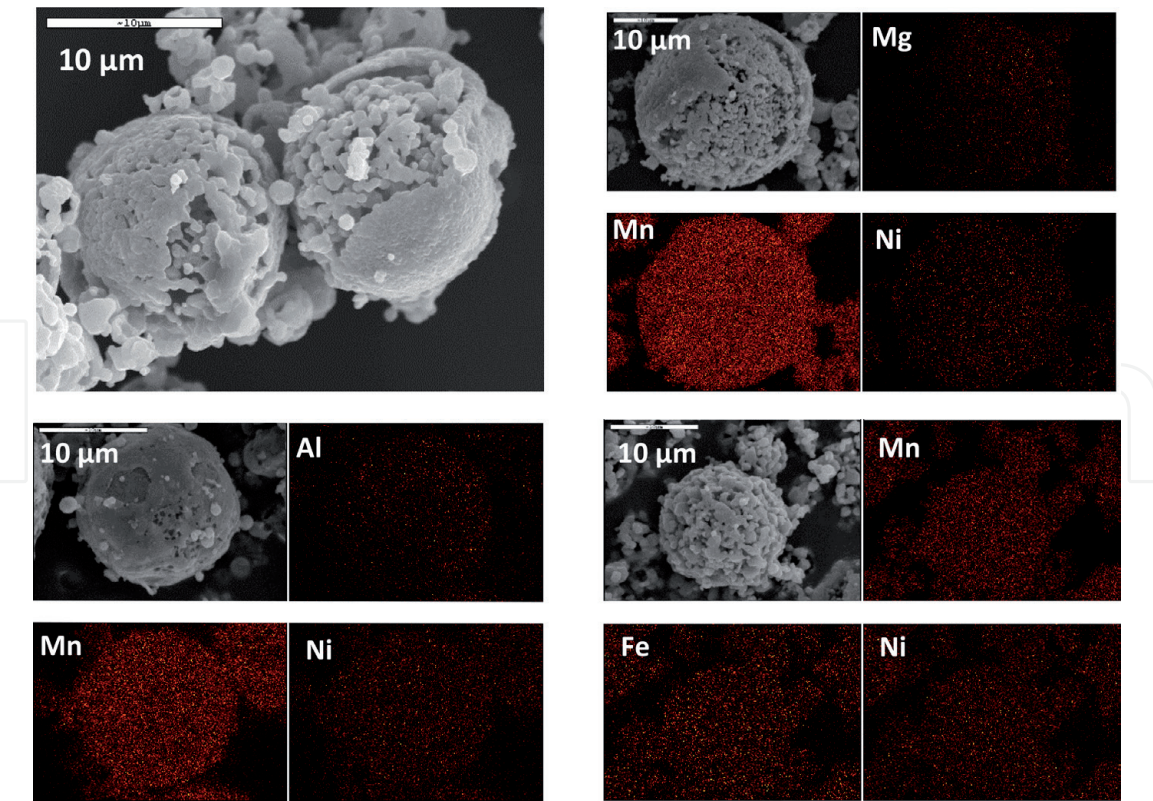


Figure 4.
SEM images and EDS mapping analysis for the pristine and doped LNMO particles.

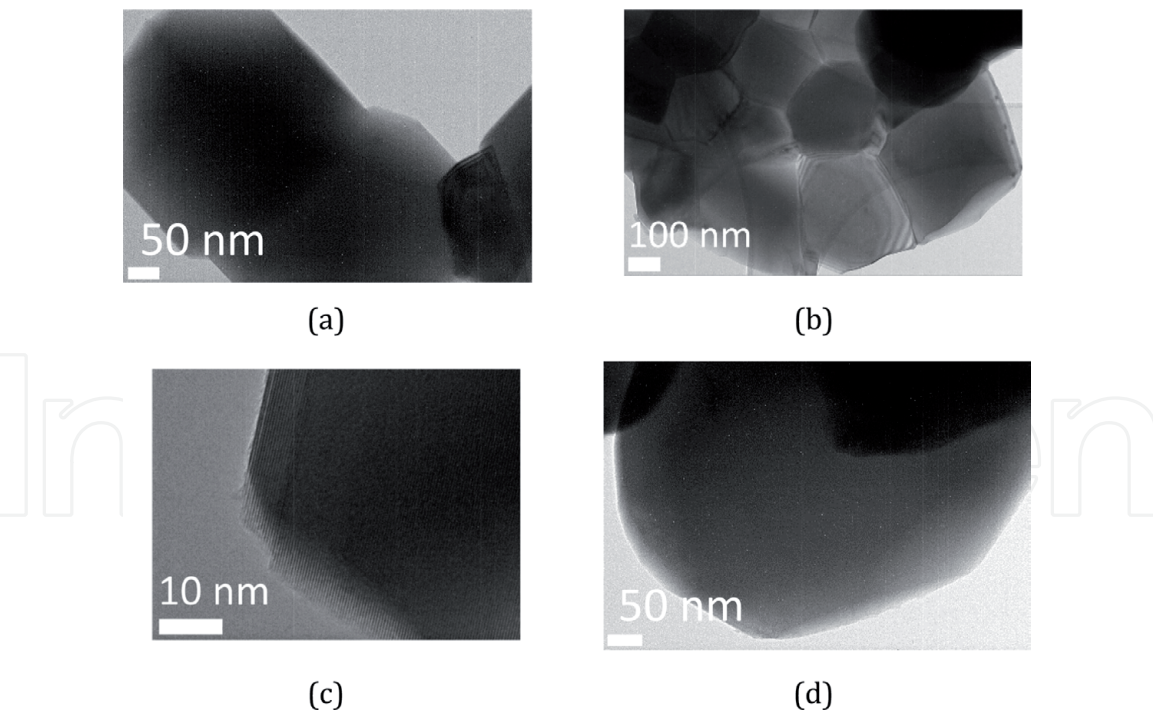


Figure 5.
TEM images depicting the crystallites of the LNMO of (a) pristine, (b) Mg-LNMO, (c) Al-LNMO and (d) Fe-LNMO.

in consistency with the XRD patterns which also confirm the homogeneity of the synthesized structures.

The morphology of the polycrystalline material obtained from the TEM images in **Figure 5** shows the aggregated morphology in the nanoscale, revealing similar morphological characteristics for all three doped compositions.

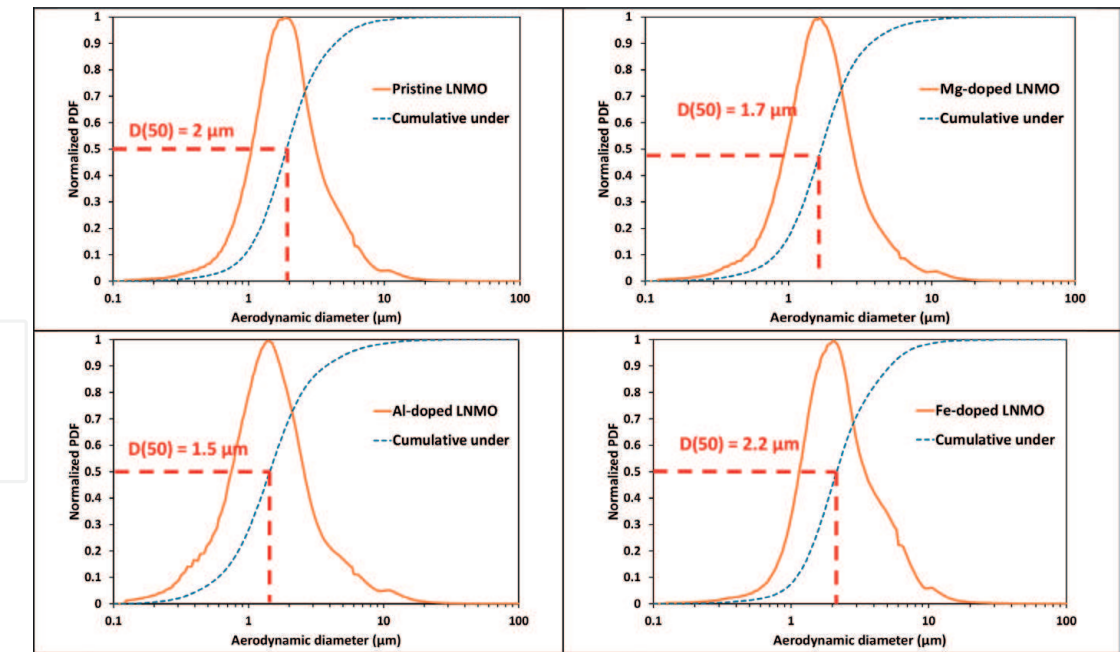


Figure 6. Particle volume probability density function distribution of the pristine and doped LNMO particles measured by an aerodynamic diameter measuring technique.

Concerning the particle size distribution analysis, the mean particle diameter of pristine material was 2 μm ; doping with Al and Mg led to smaller particle sizes while Fe doped had the higher particle size distribution at 2.2 μm , as observed in the normalized particle volume probability density function (PDF) plots of **Figure 6**.

Raman spectra was obtained in order to evaluate lattice differences of the pristine and doped LNMO materials. The spectra at **Figure 7** exhibits the 636 cm^{-1} peak, which is assigned to the Mn-O stretching vibration of the A_{1g} mode shifted to slightly higher wavenumbers due to the insertion of the Ni^{2+} ions in the spinel lattice [59]. The decrease of Ni amount (doped compositions), shifts the corresponding peak to the nominal location at 625 cm^{-1} attributed to the symmetric stretching

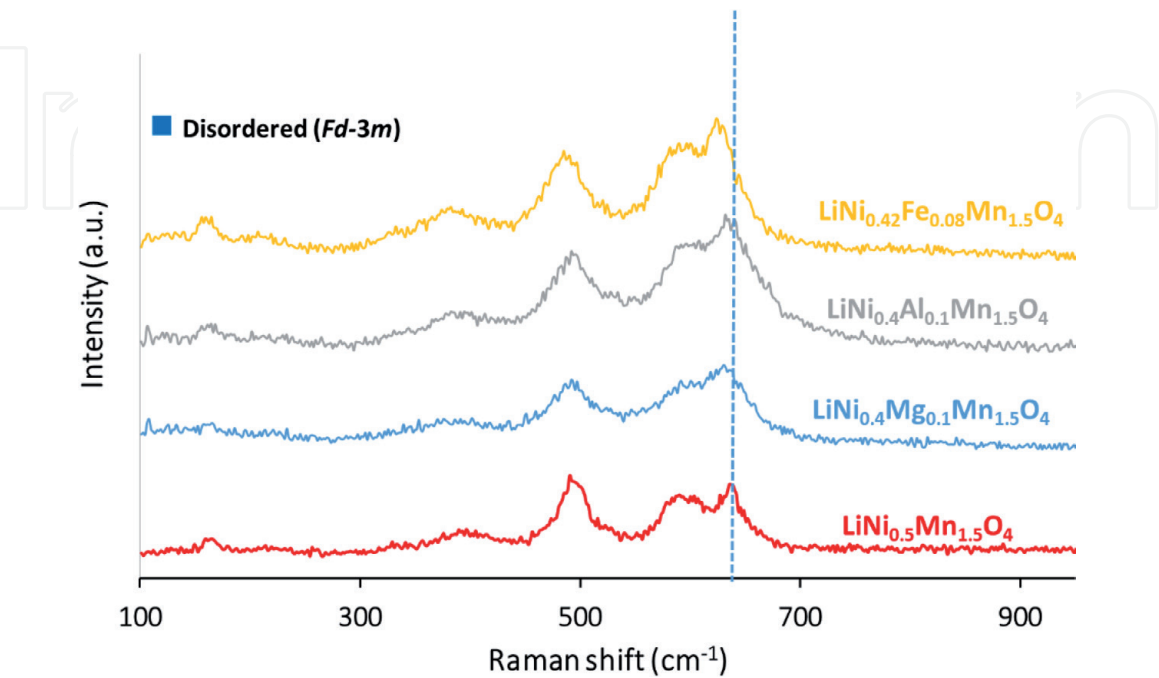


Figure 7. Raman spectrum of the doped LNMO materials.

vibration of the Mn-O of the MnO_6 groups. The broadening of the two peaks at 582 and 605 cm^{-1} , which cannot be separated in the disordered structures, is attributed to the $\text{F}_{(3)2g}$ and the intensity of the shoulder located at 580 cm^{-1} is enhanced upon nickel substitution.

5. Electrochemical characterization results

The respective LNMO doped active materials were coated on aluminum foils using different formulations of active material, carbon and binder – as explained below – in order to study the material ratios and process parameters for slurry preparation and battery performance optimization. The coated material was also tested under different calendering densities, by varying the calendering pressure and final active layer thickness. The coated electrodes were analyzed for their electrochemical performance in the form of Half Coin Cells (HCC) with a metallic Lithium foil as counter electrode and evaluating their discharge specific capacity. Preliminary electrochemical tests were performed on all four materials using HCCs (3 cells per formulation/material). Discharge C-rate varied from C/5 to 10C on comparable electrodes prepared with a formulation AM/Carbon/PVdF ratio of 90/5/5, a real loading $\sim 1.5 \text{ mAh cm}^{-2}$ and density of 2.5 g cm^{-3} .

As depicted in **Figure 8**, a profound specific discharge capacity decay was observed in both pristine and Mg-doped LNMO during cycles 1 to 5 (C/5 low rate and near-zero values were recorded until cycle 32 at high C-rates. Al-doped LNMO demonstrated high specific capacity values ($\sim 120 \text{ mAh g}^{-1}$) at low C-rates i.e. C/5, C/2, 1C while at higher discharge C-rates of 2C, 5C, 8C and 10C the specific capacity demonstrated values of ~ 110 , ~ 90 , ~ 50 and $\sim 20 \text{ mAh g}^{-1}$ respectively. The discharge specific capacity almost regained its initial high values when C-rate was decreased at C/2 during cycle 24 and withstood high charge rates ($\sim 80 \text{ mAh/g}$ at 3C charge, cycles 29–31). On the other hand, Fe-doped LNMO demonstrated similar behavior during cycles 1–8, however the performance was clearly poorer than the Al-doped LNMO composition at 2C and 5C (i.e. ~ 90 and $\sim 18 \text{ mAh g}^{-1}$ respectively) while it dropped to zero during fast discharge at 8C and 10C. During the C-rate

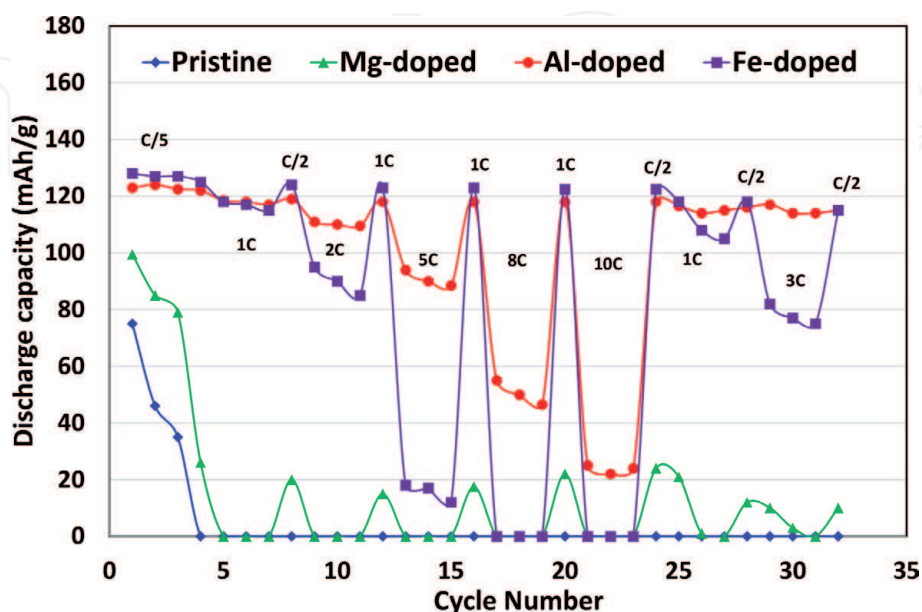
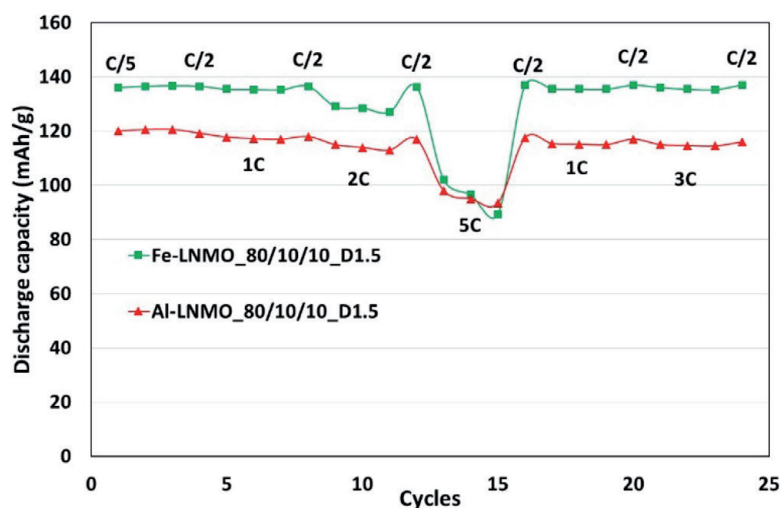
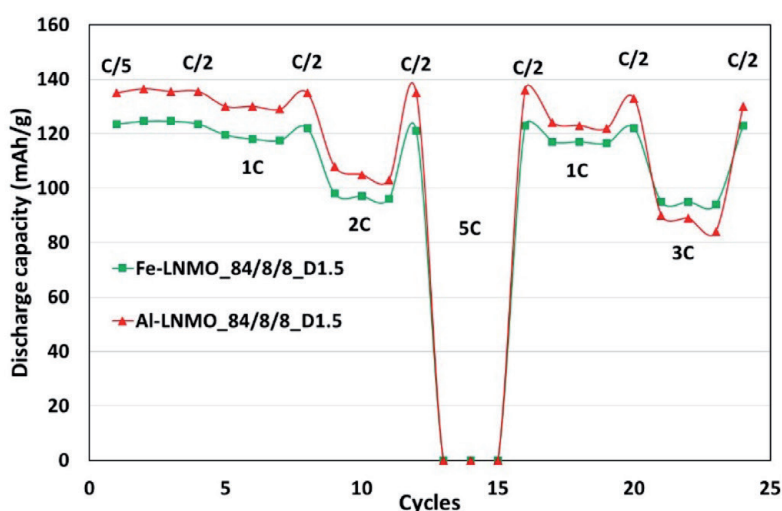


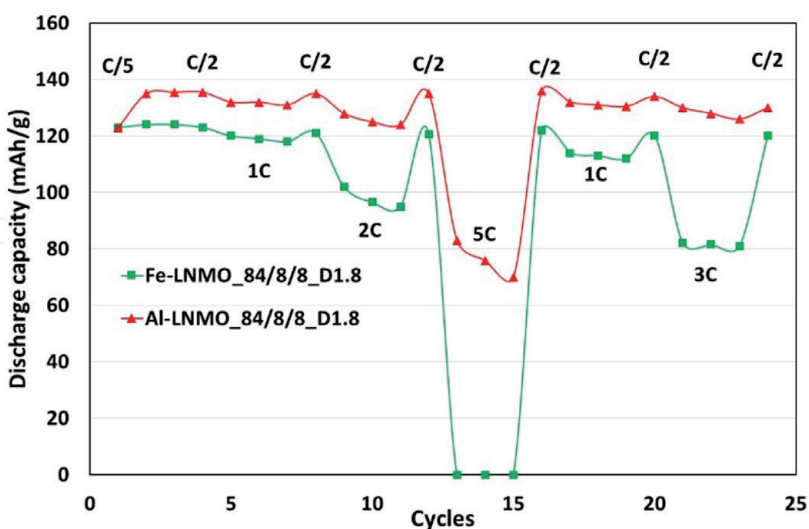
Figure 8. Specific capacity of the different doped LNMO electrodes at different discharge rates (1C to 10C) and charge rates (1C, 3C).



(a)



(b)



(c)

Figure 9.

Specific capacities of iron and aluminum doped LNMO for the same target loading of $\sim 1.0 \text{ mAh cm}^{-2}$ under different electrode formulations and densities (a) 80/10/10_D1.5, (b) 84/8/8_D1.5 and (c) 84/8/8_D1.8 (D in g cm^{-3}).

reduction at cycle 24 (C/2), an increase in specific discharge capacity to the initial values was observed but again performance was inferior to the Al-doped LNMO case throughout cycles 25–32.

Based on the abovementioned electrochemical results, Fe-doped and Al-doped LNMO were chosen for further testing in HCCs in order to study the effect of the AM/Carbon/PVdF and electrode density on the electrochemical performance.

The effect of electrode formulations with higher conducting carbon content to improve electrical conductivity and the calendaring density on electrochemical performance of Fe-doped and Al-doped LNMO is depicted in **Figure 9(a)–(c)**. The materials were tested with high C black content, an AM/carbon/PVdF ratio 80/10/10 ratio, that limited the achievable loading to 1 mAh cm^{-2} and a density of 1.5 g cm^{-3} . **Figure 9(a)** depicts low C-rates of C/5 to 1C during cycles 1–8; Fe-doped LNMO demonstrated higher values of specific discharge capacity compared to Al-doped LNMO (~ 138 and 118 mAh g^{-1} respectively), while similar performance in the range $80\text{--}100 \text{ mAh g}^{-1}$ was observed in the higher C-rate of 5C (cycles 13–15). Increasing the amount of active material to optimize the energy density of the active layer while maintaining slurry stability, achieved an AM/carbon/PVdF ratio of 84/8/8. As shown in **Figure 9(b)**, the Al-doped LNMO performance demonstrates a capacity improvement while a capacity reduction is observed in the case of Fe-doped LNMO. During cycles 1–4 (C/5 and C/2 rates) the specific capacity reaches values ~ 137 and 125 mAh g^{-1} for Al-doped and Fe-doped LNMO respectively, with further decrease at 1C rate (130 and 120 mAh g^{-1} respectively) and 2C rate (105 and 95 mAh g^{-1} respectively). Both materials demonstrate zero capacity at 5C rate. On subsequent charge at 1C during cycles 17–19, a decrease in Al-doped LNMO capacity is observed compared to 1C discharge cycles 5–7 while insignificant change in Fe-doped LNMO was observed in the course of the same cycles. During 3C charge (cycles 21–23), Fe-doped LNMO performed better than Al-doped LNMO with a specific capacity of ~ 95 vs. 85 mAh g^{-1} for the Al-doped LNMO composition.

Finally, by further increase of the density to 1.8 g cm^{-3} , a significant improvement of Al-doped LNMO performance was observed, especially at the higher C-rates of 2C, 3C and 5C in **Figure 9(c)**. On the contrary, no improvement was observed in the case of Fe-doped LNMO, as the capacity values remained almost the same as for 1.5 g cm^{-3} densification. The enhanced electrochemical activity of the Al-doped LNMO at the 1.8 g cm^{-3} density comparing to that of 1.5 g cm^{-3} shows the importance of the physicochemical properties of the overall electrode, beginning from the nanoscale of Al ion doping in the LNMO lattice to the macroscale attributed to the density of the coated electrode; the conductivity (Li-ion mobility and electrical conductivity) of the cathode increases when carbon and LNMO particle interfaces are in better contact by calendaring.

6. Conclusions

Aerosol Spray pyrolysis is a sustainable and promising route for the synthesis of anode and cathode nanostructured materials, which is exploited by research laboratories and is employed for industrial production. In the current work, $\text{LiNi}_{0.5}\text{Mn}_{1.5}\text{O}_4$ spinel was synthesized at a production rate of 100 gr hrs^{-1} and was studied for three different doping compositions of Mg, Fe and Al; $\text{LiNi}_{0.4}\text{Mg}_{0.1}\text{Mn}_{1.5}\text{O}_4$, $\text{LiNi}_{0.42}\text{Fe}_{0.08}\text{Mn}_{1.5}\text{O}_4$ and $\text{LiNi}_{0.4}\text{Al}_{0.1}\text{Mn}_{1.5}\text{O}_4$ by substituting Ni molar ratio in the spinel lattice. The aqueous precursor solutions were sprayed at a heated tubular reactor at 800°C , while further calcination of the collected powder was carried out at 850°C for 16 hrs [11]. The Raman spectra and XRD diagrams depict successful synthesis of the mixed structure, while SEM showed spherical particles with partially hollow morphology. The electrochemical evaluation was performed for different electrode formulations and loading/densities in half coin cells at different C-rates. Fe- and Al-doped materials for the electrode formulation

AM/C/PVdF = 90/5/5 exhibited high specific capacity values ($\sim 120 \text{ mAh}\cdot\text{g}^{-1}$) at low C-rates, while at higher discharge C-rates of 2C, 5C, 8C and 10C the specific capacity demonstrated values of ~ 110 , ~ 90 , ~ 50 and $\sim 20 \text{ mAh}\cdot\text{g}^{-1}$ respectively, showing interesting activity for further study, while pristine and Mg- doped material showed very low capacity at rates exceeding 1C. Fe- and Al- LNMO were further studied at lower active material ratios; namely 80/10/10 ratio using a density of $1.5 \text{ g}\cdot\text{cm}^{-3}$, where Fe-doped LNMO demonstrated higher values of specific discharge capacity compared to Al-doped LNMO at low C-rates of C/5 to 1C (~ 138 and $118 \text{ mAh}\cdot\text{g}^{-1}$ respectively), while similar performance in the range $80\text{--}100 \text{ mAh}\cdot\text{g}^{-1}$ was observed for the higher C-rate of 5C. Increasing the amount of active material to 84/8/8 to increase electrode energy density for practical battery application, improved the capacity for the Al-doped case, while a capacity reduction was observed for the Fe-doped LNMO. The current work shows the potential of Fe and Al doped LNMO synthesized by ASP as promising materials for cobalt free cathodes for the development of high voltage next generation Li-ion batteries.

Acknowledgements

We would like to thank the European Commission for funding this work through the HORIZON2020 eCAIMAN project (Grant No: GV-1-2014-653331). Dimitrios Zarvalis from CERTH is highly acknowledged for his contribution for the scaling up of the LNMO manufacturing process.

Conflict of interest

The authors declare no conflict of interest.

Abbreviations

| | |
|------|--|
| LNMO | $\text{LiNi}_{0.5}\text{Mn}_{1.5}\text{O}_4$ |
| XRD | X-Ray Diffraction |
| SEM | Scanning Electron Microscopy |
| EDS | Energy Dispersive Spectroscopy |
| TEM | Transmission Electron Microscopy |
| BET | Brunauer–Emmett–Teller |
| FWHM | Full Width Half Maximum |
| HCC | Half Coin Cell |
| AM | Active Material |
| PVdF | Polyvinylidene fluoride |
| LIB | Rechargeable Li-ion batteries |
| EV | Electric Vehicles |
| EMC | Ethyl Methyl Carbonate |
| NMP | N-methyl-2-pyrrolidone |

IntechOpen

Author details

George Ganas¹, George Karagiannakis¹, Aitor Eguia-Barrio², Miguel Bengoechea², Iratxe de Meaza^{2,3} and Georgia Kastrinaki^{1*}


¹ Chemical Process and Energy Resources Institute, CERTH, Thessaloniki, Greece

² CIDETEC, Basque Research and Technology Alliance (BRTA), Donostia-San Sebastián, Spain

³ Department of Organic and Inorganic Chemistry, Universidad del País Vasco (UPV/EHU), Bilbao, Spain

*Address all correspondence to: georgiak@certh.gr

IntechOpen

© 2022 The Author(s). Licensee IntechOpen. This chapter is distributed under the terms of the Creative Commons Attribution License (<http://creativecommons.org/licenses/by/3.0>), which permits unrestricted use, distribution, and reproduction in any medium, provided the original work is properly cited. 

References

- [1] Kuthanapillil M. Shaju and Peter G. Bruce, Nano-LiNi_{0.5}Mn_{1.5}O₄ spinel: a high power electrode for Li-ion batteries, Dalton Trans., 2008, 5471-5475
- [2] Chen G., Yang J., Tang J., Zhou X., RSC Adv. 5 (2015) 23067-23072.
- [3] J.B. Goodenough, Y. Kim, Challenges for rechargeable Li batteries, Chem. Mater. 22 (2010) 587-603.
- [4] V. Etacheri, R. Marom, R. Elazari, G. Salitra, D. Aurbach, Challenges in the development of advanced Li-ion batteries: a review, Energy Environ. Sci. 4 (2011) 3243-3262
- [5] D. Andre, S.-J. Kim, P. Lamp, S.F. Lux, F. Maglia, O. Paschos, B. Stiaszny, Future generations of cathode materials: an automotive industry perspective, J. Mater. Chem. 3 (2015) 6709-6732
- [6] Jung D. S., Ko Y. N., Kang Y.C., Park S.B., "Recent progress in electrode materials produced by spray pyrolysis for next-generation lithium ion batteries", Advanced Powder Technology 25 (2014) 18-31
- [7] Zhu Y., Choi S. H., Fan X., Shin J., Ma Z., Zachariah M. R., Choi J. W., Wang C., "Recent Progress on Spray Pyrolysis for High Performance Electrode Materials in Lithium and Sodium Rechargeable Batteries", Adv. Energy Mater. 2017, 1601578
- [8] Jang H., Seong C., Suh Y., Kim H., Lee C. Synthesis of Lithium-Cobalt Oxide Nanoparticles by Flame Spray Pyrolysis, Aerosol Science and Technology (2004), 38:10, 1027-1032, DOI: 10.1080/027868290524016
- [9] Abram C, Shan J., Yang X., Yan C., Steingart D., Ju Y., "Flame Aerosol Synthesis and Electrochemical Characterization of Ni-Rich Layered Cathode Materials for Li-Ion Batteries", ACS Appl. Energy Mater. 2019, 2, 1319-1329
- [10] Madero J. E., Li J., Shen K.-Y., Wojtak J., Axelbaum R.L., "An approach to low-temperature flame spray pyrolysis for the synthesis of temperature-sensitive materials: Application to Li_{1.2}Mn_{0.54}Ni_{0.13}Co_{0.13}O₂", Applications in Energy and Combustion Science 5 (2021) 100020
- [11] Ganas, G., Kastrinaki, G., Zarvalis, D., Karagiannakis, G., Konstandopoulos, A.G., Versaci, D., Bodoardo, S., "Synthesis and Characterization of LNMO Cathode Materials for Lithium-ion Batteries", Materials Today: Proceedings 5 (2018) 27416-27424
- [12] Shimoi N., "Synthesis of anode active material particles for lithium-ion batteries by surface modification via chemical vapor deposition and their electrochemical characteristics", Adv. Powder Technol. (2017)
- [13] Ogihara T., Ogata N., Katayama K., Azuma Y., Mizutani N., Electrochemistry 68 (2000) 162-166
- [14] Pateya T.J., Büchelb R., Nga S.H., Krumeich F., Pratsinis S.E., Nováka P., Flame co-synthesis of LiMn₂O₄ and carbon nanocomposites for high power batteries", Journal of Power Sources 189 (2009) 149-154
- [15] Saft M., Chagnon G., Faugeras T., Sarre G., Morhet P., J. Power Sources 80 (1999), 180-189
- [16] Y. Tanjo, T. Abe, H. Horie, T. Nakagawa, T. Miyamoto, K. Katayama, Soc. Automot. Eng. (Spec. Publ.) SP-1417 (1999) 51-55
- [17] Bresser D., Paillard E., Copley M., Bishop P., Winter M., Passerini S., "The

importance of “going nano” for high power battery materials”, *Journal of Power Sources* 219 (2012) 217-222

[18] Lorentzou S., Kastrinaki G., Pagkoura C., Konstandopoulos A.G. “Oxide Nanoparticles for Hydrogen Production from Water-splitting and Catalytic Oxidation of Diesel Exhaust Emissions”, 2011, *Nanoscience and Nanotechnology Letters*, 3 (4)

[19] Kastrinaki G., Lorentzou S., Karagiannakis G., Rattenbury M., Woodhead J., Konstandopoulos A.G. (2018) "Parametric Synthesis Study of Iron Based Nanoparticles via Aerosol Spray Pyrolysis route", *Journal of Aerosol Science*, 115, pp. 96-107

[20] Nie P., Xu G., Jiang J., Dou H., Wu Y., Zhang Y., Wang J., Shi M., Fu R., Zhang X., “Aerosol-Spray Pyrolysis toward Preparation of Nanostructured Materials for Batteries and Supercapacitors”, *Small Methods* 2018, 2, 1700272

[21] T.B. Reddy, D. Linden, *Linden's Handbook of Batteries*, fourth ed., McGraw-Hill, New York, 2011.

[22] M. Winter, J.O. Besenhard, M.E. Spahr, P. Novák, *Adv. Mater.* 10 (1998) 725-763.

[23] J.M. Tarascon, M. Armand, *Nature* 414 (2001) 359,

[24] J.B. Goodenough, Electrochemical cell with new fast ion conductors, US patent No. 4302518A, 1981, US.

[25] M. Wakihara, O. Yamamoto, *Lithium ion batteries: fundamentals and performance*, Wiley-VCH, New York, 1998.

[26] C. Miao, P.F. Bai, Q.Q. Jiang, X.Y. Wang, *J. Power Sources* 246 (2014) 232-238.

[27] D. Zhao, Y.L. Feng, Y.G. Wang, Y.Y. Xia, *Electrochim. Acta* 88 (2013) 632-638.

[28] D. Liu, W. Zhu, J. Trottier, F. Gagnon, C.M. Julien, J.B. Goodenough, K. Zaghib, *RSC Adv.* 4 (2014) 154-167

[29] R. Santhanam, B. Rambabu, J. Power Sources 195 (2010) 5442-5451

[30] Patoux, L. Daniel, C. Bourbon, C. Pagano, S. Jouanneau, S. Martinet, *J. Power Sources* 189 (2009) 344-352

[31] S.H. Oh, K.Y. Chung, S.H. Jeon, C.S. Kim, W.I. Cho, B.W. Cho, *J. Alloys Comp.* 469 (2009) 244-250

[32] M.G. Kim, J. Cho, *Adv. Funct. Mater.* 19 (2009) 1497-1514

[33] N.P.W. Pieczonka, Z. Liu, P. Lu, K.L. Olson, J. Moote, J.-H. Kim, *J. Phys. Chem. C* 117 (2013) 15947-15957.

[34] L. Wang, D. Chen, J. Wang, G. Liu, W. Wu, G. Liang, *Powder Technology* 292 (2016) 203-209

[35] Y. Xue, Z. Wang, F. Yu, Y. Zhang, G. Yin, *J. Mater. Chem. A* 2 (2014) 4185-4191.

[36] Qin, X., Gong, J., Guo, J., Zong, B., Zhou, M., Wang, L., Liang, G., *Journal of Alloys and Compounds* 786 (2019) 240-249

[37] Y.J. Gu, Y. Li, Y. Fu, Q.F. Zang, H.Q. Liu, J.X. Ding, Y.M. Wang, H.F. Wang, J. Ni, *Electrochim. Acta* 176 (2015) 1029-1035

[38] Shen, Y., Ju, X., Zhang, J., Xie, T., Zong, F., Xue, D., Lin, X., Zhang, J., Li, Q., *Materials Chemistry and Physics* 240 (2020) 122137

[39] Ren, X., Wang, Y., Xiao, Q., Lei, G., Li, Z., *Material Letters* 248 (2019) 97-100

[40] Li, Y., Wang, J., Yao, Q., Wang, Z., Zhou, H., Deng, J., *Int. J. Electrochem. Sci.*, Vol. 14, 2019

- [41] H.B. Lin, Y.M. Zhang, H.B. Rong, S.W. Mai, J.N. Hu, Y.H. Liao, L.D. Xing, M.Q. Xu, X.P. Li, W.S. Li, *J. Mater. Chem. A* 2 (2014) 11987-11995
- [42] Rahim, A.S, Aziz, N., Nor, A.M., Osman, Z., *Molecular Crystals and Liquid Crystals*, 695 (1) (2019) 10-18
- [43] Sone, H., Yoshida, S., Tanaka, M., Watanabe, T., *Journal of the Ceramic Society of Japan* 128 (9) 635-640 2020
- [44] G. Liu, X. Kong, H. Sun, B. Wang, *Ceram. Int.* 40 (2014) 14391-14395
- [45] L. Wen, Q. Lu, G. Xu, *Electrochim. Acta* 51 (2006) 4388-4392.
- [46] J.H. Kim, S.T. Myung, Y.K. Sun, *Electrochim. Acta* 49 (2004) 219-227
- [47] Zarvalis D., Gkanas G., Kastrinaki G., Karagiannakis G., Konstandopoulos A.G., Eguia-Barrio A., Bengoechea M., de Meatza I., Ahniyaz A., Bourbon C., Fabre F., Peralta D, "LNMO cathode materials for high-voltage, next -generation automotive Li-ion cells", *Proceedings of 7th Transport Research Arena (TRA 2018)*, *Proceedings of 7th Transport Research Arena (TRA 2018)*.
- [48] H. Zhang, Y. Xu, D. Liu, X. Zhang, C. Zhao. *Electrochim. Acta* 125 (2014) 225-231
- [49] Q. Liu, S. Wang, H. Tan, Z. Yang, J. Zeng. *Energies* 6 (2013) 1718-1730.
- [50] S. Bao, W. Zhou, Y. Liang, B. He, H. Li. *Mater. Chem. Phys.* 95 (2006) 188-192.
- [51] C. Locati, U. Lafont, L. Simonin, F. Ooms, E. Kelder. *J. Power Sources* 174 (2007) 847-851.
- [52] U. Lafont, C. Locati, W.J.H. Borghols, A. Lasinka, J. Dygas, A.V. Chadwick, E.M. Kelder. *J. Power Sources* 189 (2009) 179-184.
- [53] M. Wagemaker, F.G.B. Ooms, E.M. Kelder, J. Schoonman, G.J. Kearley, F.M. Mulder. *J. Am. Chem. Soc.* 126 (2004) 13526-13533.
- [54] S.T. Myung, S. Komaba, N. Kumagai. *J. Electrochem. Soc.* 148 (2001) A482-A489.
- [55] Y.K. Sun, C.S. Yoon, C.K. Kim, S.G. Youn, Y.S. Lee, M. Yoshio, I.H. Oh. *J. Mater. Chem.* 11 (2001) 2519-2522.
- [56] G.B. Zhong, Y.Y. Wang, Z.C. Zhang, C.H. Chen. *Electrochim. Acta* 56 (2011) 6554-6561.
- [57] Asxaxs R. Alcantara, M. Jaraba, P. Lavela, J.M. Lloris, C.P. Vicente, J.L. Tiradoz. *J. Electrochem. Soc.* 152 (2005) A13-A18.
- [58] J. Liu, A. Manthiram, *J. Phys. Chem. C* 113 (2009) 15073
- [59] Zhang, X.; Cheng, F.; Zhang, K.; Liang, Y.; Yang, S.; Liang, J.; Chen, J. Facile polymer-assisted synthesis of $\text{LiNi}_{0.5}\text{Mn}_{1.5}\text{O}_4$ with a hierarchical micro-nano structure and high rate capability. *RSC Adv.* 2012, 2, 5669-5675.